Biosensors and Bioelectronics 133 (2019) 250–257

Contents lists available at ScienceDirect

Biosensors and Bioelectronics

journal homepage: www.elsevier.com/locate/bios

3D hierarchical hollow hydrangea-like Fe^{3+}@ε-MnO_2 microspheres with excellent electrochemical performance for dopamine and hydrogen peroxide

Haiyan Song[a,b], Hui Zhao[a], Xianfa Zhang[a], Yingming Xu[a,*], Xiaoli Cheng[a], Shan Gao[a], Lihua Huo[a,*]

[a] Key Laboratory of Functional Inorganic Material Chemistry, Ministry of Education, School of Chemistry and Materials Science, Heilongjiang University, Harbin 150080, China
[b] Laboratory of Test Center, Jilin Agricultural Science and Technology College, Jilin 132101, China

ARTICLE INFO

Keywords:
Hydrangea-like Fe^{3+}@ε-MnO_2
Hierarchical hollow structure
DA
H_2O_2
Electrocatalysis

ABSTRACT

Construction a sensor to accurately detect dopamine (DA) and hydrogen peroxide (H_2O_2) is meaningful due to their close relation to the health of organisms. In this work, one-step hydrothermal method was employed to synthesize hierarchical hollow hydrangea-like Fe^{3+}@ε-MnO_2 microspheres constructed by interconnected nanosheets, and the growth mechanism of the microspheres (n_{Fe}/n_{Mn} = 0.6) was also investigated in detail. The material was used to construct an electrochemical sensor for DA and H_2O_2 detection with the linear range of 0.02–78 μmoL^{-1} and 0.000133–5.19 mmoL^{-1}, respectively. The detection limit and sensitivity for DA and H_2O_2 are 5 and 50 nmoL^{-1} (S/N = 3), 7034.1 and 242.6 μA m(mol·L^{-1})$^{-1}$ cm^{-2}, respectively. Furthermore, the sensor was successfully applied to the detection of DA and H_2O_2 in serum and urine samples, indicating a potential value of this work in the pharmaceutical and environmental fields.

1. Introduction

Dopamine (DA), an important hormone and neurotransmitter belonging to the families of catecholamine and phenethylamine, is extensively presented in brain tissues as well as body fluids of all the mammals (Jin et al., 2018). It plays an important role in central nervous system, hormonal system and several physiological functions concerning to mood, behavior and so on (Zhang et al., 2018; Lin and Beal, 2006). The changes of DA levels can be used as an indicator of certain neurological diseases, such as Schizophrenia, Alzheimer's, Parkinson's, etc. (Rao et al., 2016; He et al., 2018). Hydrogen peroxide (H_2O_2), a common peroxide, is extensively applied to the pharmaceutical industries, environmental protection, clinical research, food and other procedures (Revathi and Rajendra Kumar, 2017; Kumar et al., 2018). It is produced not only in chemical and industrial processes, but also as by-product of several oxidative metabolic pathways in human body (Song et al., 2014). However, some diseases are usually induced as a result of the over production or accumulation of H_2O_2 in living cells, for instance, Alzheimer's and Parkinson's mentioned above (Wu et al., 2018; Sha et al., 2018). Therefore, developing of accurate and fast method for the determination of DA and H_2O_2 has been significant in various fields. Taking response time, cost, sensitivity, selectivity and other factors into consideration, the electrochemical technique has become more and more popular (Thanh et al., 2017 a; Thanh et al., 2017 b). In view of complicated construction process, poor stability and shorter lifetime of conventional biomacromolecule including enzymes and proteins sensors (Dai et al., 2018; Song et al., 2013; Tran et al., 2018), the sensors based on transition metal oxides nanomaterials have received rare increasing attention.

Manganese oxide (MnO_2), a capable transition metal oxide, has been deemed as a kind of potential electrochemical materials because of the slight toxicity, superior structural flexibility as well as natural abundance (Lin et al., 2016). Although it has been widely used as an electrode material in electrochemical field, the intrinsically poor electrical conductivity of MnO_2 is a major obstacle which limits its application. In this respect, a host of efforts have been focused on combination of MnO_2 with high conductive substance including conducting polymers, graphene and its derivatives. However, recent investigation showed that some heterogeneous atoms doped into lattice of MnO_2 would more essentially solve this problem in comparison with the improvement of conductivity through simply combination of different materials mentioned above (Wang et al., 2016). Moreover, large electroactive surface area and fast electron transport rate are indispensable for an excellent electrochemical material, and thus more efforts have

* Corresponding authors.
E-mail addresses: xuyingming@hlju.edu.cn (Y. Xu), huolihua@hlju.edu.cn (L. Huo).

https://doi.org/10.1016/j.bios.2019.03.017
Received 8 January 2019; Received in revised form 1 March 2019; Accepted 10 March 2019
Available online 11 March 2019
0956-5663/

been focused on the construction of MnO_2 with large specific surface area and porosity. Up to date, MnO_2 with 3D complex structures, such as nanoflowers (Li et al., 2017), microspheres (Li et al., 2005) and dandelion- and urchin-like (Zheng et al., 2017), which using zero-dimensional (0D) nanoparticles (Jaiswal et al., 2017), one-dimensional (1D) nanotubes (Sinha et al., 2018), nanorods (Saraf et al., 2018), nanowires (Chi et al., 2019), and two-dimensional (2D) nanosheets (Xiao et al., 2018) as building blocks, possess more superior performance in supercapacitor, oxygen reduction reaction, Li-ion batteries and adsorption. However, the application of MnO_2 in electrocatalysis is mainly focused on nanosheets to our best knowledge, in which the lowest detection limits of DA and H_2O_2 are approximately around 10^{-8} mol·L^{-1} and 10^{-7} mol·L^{-1} (Liu et al., 2018; Dong et al., 2015). Compared with other metal oxides sensors, there is still a great potential in improvement of catalytic performance to DA and H_2O_2 for MnO_2. According to the published literatures, MnO_2 microspheres with metal ion doping have shown excellent performance in supercapacitor and adsorption compared with pure MnO_2 (Wang et al., 2016; Pargoletti et al., 2016). Among them, the performance of iron doped-microsphere is the most outstanding, which may be caused by two reasons. On one hand, the similar atomic radius of Fe^{3+} and Mn^{4+} is beneficial for Fe^{3+} to substitute Mn^{4+} or occupy the tunnels of MnO_2. On the other hand, stable microstructure is more easily formed by the balancing of surplus protonation with the incorporating of Fe^{3+} into the framework of MnO_2. The rational heterogeneity and stable morphology laid the foundation for excellent performance. Therefore, the aim of this work was to synthesize a kind of Fe^{3+}-dopped MnO_2 microspheres with excellent conductivity, larger electroactive surface area and higher porosity, then applied them to the electrocatalysis of small molecules like DA, H_2O_2 and others.

In the present work, we reported hierarchical Fe^{3+}@ε-MnO_2 hollow microspheres which were produced via simple one-step hydrothermal method without using of templates. The morphology as well as the crystalline phase of MnO_2 were both changed following with the incorporation of Fe^{3+} into MnO_2 framework. The hollow Fe^{3+}@ε-MnO_2 microspheres with high conductivity and large electroactive surface area were employed to construct an electrochemical sensor for DA and H_2O_2 detection in phosphate buffer (pH = 7.4) without interference of the coexistence components such as ascorbic acid (AA) and uric acid (UA). This is the first report that DA and H_2O_2 were determined by the use of hierarchical hollow Fe^{3+}@ε-MnO_2 microspheres constructed sensor via electrocatalysis method with rapidity, high sensitivity and selectivity.

2. Experimental

2.1. Regents

The analytical grade reagents of $MnSO_4{\cdot}H_2O$, $AgNO_3$, $Fe(SO_4){\cdot}7H_2O$ and $(NH_4)_2S_2O_8$ were all bought from Beijing Chemical Reagent Co., Beijing, China; AA, UA, DA and chitosan (CS) were purchased from Sigma Aldrich Co., USA. Adrenaline, Histamine, Epnephrine, Serotonin, Tyramine and Phenethylamine were purchased from Shanghai Titan Scientific Co., Shanghai, China. Dilute H_2O_2 aqueous was prepared when it was used. Phosphate buffer (0.05 mol·L^{-1}, pH 7.4) consisted of KH_2PO_4 and K_2HPO_4 was used as the supporting electrolyte.

2.2. Instrumentation

X-ray diffraction meter was employed to investigate the hollow Fe^{3+}@ε-MnO_2 microspheres. Bragg angle ranges from −10 to 80°. (XRD, D/MAX-III-B-40 kV, Japan, Cu Kα radiation, λ = 0.15406 nm).

Microstructure and elemental mapping of hollow Fe^{3+}@ε-MnO_2 microspheres were investigated by scanning electron microscope (SEM; Hitachi S-4800, Hitachi, Japan, 15.0 kV). Transmission electron microscopy (TEM), high-resolution TEM (HRTEM) and selected area electron diffraction (SAED) were used for further analysis of the samples (JEOL-2100, JEOL Co., Japan, 200 kV).

The specific surface areas and pore-size distributions were determined by N_2 adsorption apparatus (BET, Tristar II 3020, USA) using the Brunauer-Emmett-Teller (BET) and the Barrett-Joyner-Halenda (BJH) methods, respectively.

Valence state of the sample was analyzed by X-ray photoelectron spectra within ± 0.2 eV deviation in the binding energy position (XPS, Kratos Amicus, Manchestert, England, Al Kα radiation, hν = 1486.6 eV).

All the electrochemical tests were conducted on a electrochemical workstation (CHI-760E, Shanghai Chenhua Apparatus Co., Shanghai, China) equipped with standard three-electrode system, in which the diameter of modified glassy carbon electrode (working electrode) was 5 mm; the auxiliary electrode and reference electrode were platinum wire and saturated calomel electrode (SCE), respectively.

2.3. Synthesis of hierarchical hollow Fe^{3+}@ε-MnO_2 microspheres

The hierarchical hollow Fe^{3+}@ε-MnO_2 microsphere was synthesized using a simple one-step hydrothermal method. In brief, $MnSO_4{\cdot}H_2O$ (0.270 g), $(NH_4)_2S_2O_8$ (0.365 g) and 1.6 mL of con. H_2SO_4 were added to 40 mL of deionized water at room temperature. Then, 0.8 mL of $AgNO_3$ (5.9 mol·L^{-1}) solution was added into the above solutions. Afterwards, a certain amount of $FeSO_4{\cdot}7H_2O$ (n_{Fe}/n_{Mn} = 0.4, 0.5, 0.6 and 0.7) was also introduced to the above mixture. Time interval for each stirring was lasted for 30 min, the resulting solution was put into Teflon-lined stainless steel autoclave with a volume of 50 mL. Subsequently, the steel autoclave was heated for 6 h under the temperature of 120 °C. When the reaction was finished, the products were collected by centrifugation, then washed using deionized water and ethanol, and dried for 12 h at the temperature of 80 °C in an oven.

2.4. Preparation of different modified glassy carbon electrodes

10 μL of hollow hydrangea-like Fe^{3+}@ε-MnO_2 microspheres distributed in ethanol with concentration of 2 mg·mL^{-1} was slowly dropped onto the surface of a polished and activated glassy carbon electrode. Subsequently, 5 μL of 2% (wt.) chitosan solution was added onto the surface of the electrode mentioned above. Each drop-coated material for electrode modification must be dried in air. The rest modified electrodes were all constructed by using the corresponding dispersion materials. The pretreatment process of glassy carbon electrode is listed in S1-1 (Supplementary materials). In addition, the determination conditions including applied potential (Fig. S1), pH (Fig. S2) and temperature (Fig. S3) were also investigated based on the selection of n_{Fe}/n_{Mn} (Fig. S4).

3. Results and discussion

3.1. Characterization of the composites

The surface element information (such as valance state and composition) of the material was obtained through the XPS (Fig. 1A) analysis. As shown in Fig. 1A, the Fe 2p spectrum shows two main peaks at 723.7 (Fe $2p_{1/2}$) and 711.1 eV (Fe $2p_{3/2}$), which do not exist the overlapping of the binding energy. The satellite peaks of Fe $2p_{1/2}$ and Fe $2p_{3/2}$ appeared at 728.4 and 717.9 eV can be observed clearly, indicating the valence state of Fe in the sample is + 3. Focusing on the Mn 2p spectrum, two different oxidation states (Mn^{4+} and Mn^{3+}) can be distinctly found (Fig. 1B). The ratio of Mn^{4+}/ Mn^{3+} is 0.32/0.68. All these prove that the Fe^{2+} added to the system were completely oxidized to Fe^{3+} by MnO_2.

XRD technique was employed to identify the crystal phase and

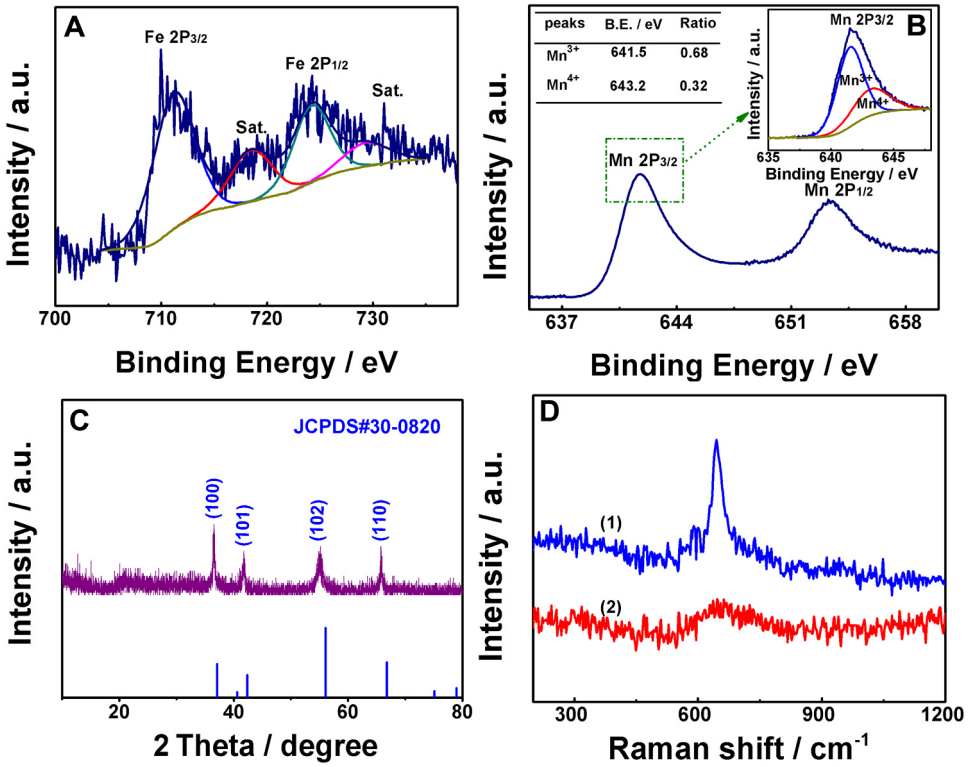

Fig. 1. XPS spectra of Fe_{2p} (A) and Mn_{2p} (B); XRD (C) and Raman spectra (D): (1) α-MnO_2; (2) Fe^{3+}@ε-MnO_2 synthesized at 120 °C for 6 h (n_{Fe}/n_{Mn} = 0.6).

purity of the sample obtained at 120 °C for 6 h (n_{Fe}/n_{Mn} = 0.6). According to the previous report, diffraction peaks of the XRD might shift to smaller angles when the crystal framwork was incorporated by the metal ions with larger radius (Wang et al., 2016). As can be seen from Fig. 1C, the only four diffraction peaks, where no any other peaks belong to iron oxide, all shift to smaller angles compared with the standard ε-MnO_2 (JCPDS 30–0820), indicating Fe3+ has been uniformly incorporated into lattice of MnO2. It is caused by the doping of Fe^{3+} (0.69 Å) which has a larger radius than Mn^{4+} (0.67 Å) in six coordination into MnO_2. The diffraction peaks of 36.2°, 41.9°, 55.3° and 66.1° correspond to the (100), (101), (102) and (110) planes of ε-MnO_2, separately. To obtain more detailed information about the changing of crystal structure of above material, the typical Rietveld refinement was employed. As shown in Fig. S5, the calculated profile is in good agreement with the observed patterns when the R_p (%), R_{wp} (%) and X^2 are 3.143, 3.965 and 1.732, respectively. The comparison of refined lattice parameters of Fe^{3+}@ε-MnO_2 (n_{Fe}/n_{Mn} = 0.6) and standard ε-MnO_2 (JCPDS 30–0820) are listed in Table S1. From the table we can see, the cell volume of Fe^{3+}@ε-MnO_2 (36.4073 $Å^3$) is increased compared with the ε-MnO_2 (34.888 $Å^3$). This result successfully proves the point that the doping Fe^{3+} with a larger ionic radius can lead to swelling of crystal structure. To further verify the conclusion that crystal framwork was doped with iron ions, the Raman spectra of the samples were also tested through the contrast of lattice vibrational behavior before and after doping. As displayed in Fig. 1D, the peak of pure α-MnO_2 located at 650–660 cm^{-1}, can be attributed to the lattice vibration of O-Mn-O (curve 1). In contrast to that, no extra vibrational peaks obtained from any Fe-O bond can be found after Fe is incorporated into ε-MnO_2 (curve 2), except that a broadened peak appeared at 650 cm^{-1} can be observed clearly. It reveals the smaller size and poorer crystallinity of the microspheres sample, which will be discussed in detail in the following section. In a word, all the results mentioned above indicate that the material of Fe^{3+}@ε-MnO_2 has been synthesized successfully.

The information related to structure, morphology and size of the synthesized product can be obtained from different characteristic methods. As shown in SEM (Fig. 2A), most microspheres show the hydrangea-like shape and the diameters are mostly concentrated in 700–900 nm. The cross-linked nano-sheets can be observed clearly by the zooming in a single microsphere (Fig. 2B (left)). The diameter of the microsphere and the thickness of the nano-sheet are approximately 900 nm and 10 nm, and the growth mechanism is described in S1–2 (Supplementary materials) and Fig. S6–7. Elemental mapping obtained from EDX analysis shows that Mn, Fe and O are distributed on the surface of films homogeneously (Fig. 2B (right)), which is also a indirect proof that some Mn^{4+} in MnO_2 lattice have been replaced by Fe^{3+} successfully. The hollow structure is further confirmed by TEM analysis (Fig. 2C), which is resulted from intertwined nanosheets. Meanwhile, the conclusion on diameter of the microsphere and thickness of the nano-sheet is consistent with that of SEM. As shown in HRTEM pattern from a single nano-sheet (Fig. 2D), the lattice spacing of 0.244 nm may correspond to the (100) planes of the ε-MnO_2 due to the broaden of lattice spacing resulted from swell of crystal structure after incorporation of Fe^{3+}, the similar phenomenon has been reported (Niu et al., 2018). And four diffraction rings of SAED pattern (inset of Fig. 2D) are well matched with the (100), (101), (102) and (110) planes of ε-MnO_2. These results are also consistent with that of XRD analysis.

In order to further explore the porous structure and specific surface area of hollow Fe^{3+}@ε-MnO_2 microspheres, N_2 adsorption/desorption measurements were conducted (Fig. S8A). According to the IUPAC classification, the Fe^{3+}@ε-MnO_2 exhibits a type IV isotherm with H3 type hysteresis loop. The pore size distribution curve of Fe^{3+}@ε-MnO_2 shows that the main pore sizes are 10 nm and 130 nm. BET specific surface area is 54.01 m^2g^{-1} which is larger than that of undoped microsphere MnO_2 (42.23 m^2g^{-1}) (Fig. S8B). The difference might be attributed to their various structures, in which the former is hollow microsphere constructed by ultrathin nano-sheets, whereas the latter is

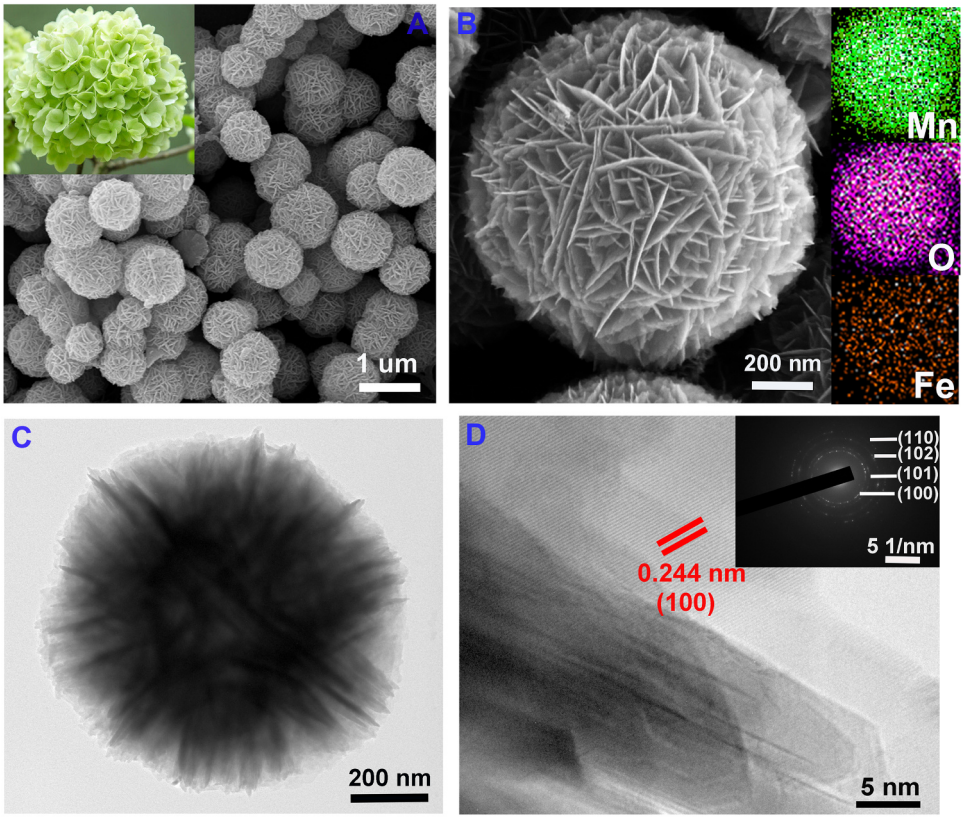

Fig. 2. (A) SEM and picture of hydrangea (inset of A); (B) enlarged SEM (left) and corresponding EDS mapping (right); (C) TEM; (D) HRTEM and SAED (inset of D) of the Fe^{3+}@ε-MnO_2 synthesized at 120 °C for 6 h ($n_{Fe}/n_{Mn}=0.6$).

urchin-like solid microsphere (Fig. S6A) which is piled up with bigger diameter nanowires (30–40 nm) accompanied by serious agglomeration. Therefore, Fe^{3+}@ε-MnO_2 might be a promising candidate for excellent sensing material due to incorporation of Fe^{3+}.

3.2. Electrochemical properties of the constructed electrodes

The electrochemical characterization of electrodes can be investigated by different methods. Interface properties of different electrodes can be obtained from electrochemical impedance spectroscopy (EIS). The semicircle diameter appeared at higher frequencies relates to procedures concerning to electron transfer-limited, in which the diameter of the semicircular plot is dependent on electron-transfer resistance. As displayed in Fig. 3A, after the electrode is modified, the electron transfer resistance varies accordingly. A plot with effectively linear can be clearly found using GCE (Fig. 3A, curve a). In order to explore the effect of Fe^{3+} doping on conductivity of microsphers material, the EIS graphs of Fe^{3+}@ε-MnO_2 and undoped MnO_2 were also investigated. The semicircle of the Fe^{3+}@ε-MnO_2/GCE (Fig. 3A, curve b) decreases significantly compared with α-MnO_2/GCE (Fig. 3A, curve c). The reason may be the doping of Fe^{3+} enhances the conductivity of the MnO_2 (Wang et al., 2016), which has been identified by the corresponding bode plots of EIS (Fig. S9). The same conclusions can be further confirmed by the cyclic voltammograms (CV) experiments (Fig. 3B).

Chronocoulometric plots, collected from the reduction of $K_3Fe(CN)_6$ (1.0 mmol·L^{-1}) in KCl (2.0 mol·L^{-1}), were used to calculate the apparent electrode areas of different electrodes. The corresponding equation is (Eq. (1)) (Dong and Zhang, 2018):

$$Q = \frac{2nFAcD^{1/2}t^{1/2}}{\pi^{1/2}} + Q_{dl} + Q_{ads} \quad (1)$$

where Q represents the absolute value of reduction charge, n presents electrons transfer number, F is the Faraday constant, A is apparent electrode area and t is time; c is the bulk concentration of oxidized form of the hexacyanoferrate (III) complex, while D is the corresponding diffusion coefficient in comparison to C (7.6×10^{-6} $cm^2 \cdot s^{-1}$); Q_{dl} is double-layer charge and Q_{ads} is Faradic charge. The apparent electrode area (A) can be calculated via the slope of Q versus $t_{1/2}$ plot. It can be seen from Fig. 3C that the slope values increase following with the order of GCE, α-MnO_2/GCE and Fe^{3+}@ε-MnO_2/GCE and corresponding values are 0.08, 0.17 and 0.27 cm^2. The effective surface area of Fe^{3+}@ε-MnO_2/GCE is about 3.4 times larger than that of GCE, indicating that Fe^{3+}@ε-MnO_2 composites may exhibit a promising electrochemical performance due to the lager value of A.

3.3. Electrocatalysis of DA at the Fe^{3+}@ε-MnO_2/GCE

To investigate the catalytic performance of Fe^{3+}@ε-MnO_2/GCE, the amperometric experiments to different aliquots of DA were operated in phosphate buffer (pH 7.4) under continually stirred at 0.4 V (Fig. 4A). The sensor shows excellent current performance in the range of 0.02–78 μmol·L^{-1} with a high sensitivity of 7034.1 μA m(mol·L^{-1})$^{-1}$ cm^{-2} (Fig. 4B). The detection limit is 5 nmol·L^{-1} (S/N = 3). When DA is brought into the electrochemical cell, the steady-state current almost achieves 90% level only within 2.8 s. After fast-dilution, it recovers to 10% of the base line less than 2.2 s (Fig. 4C). The performance of the as-prepared sensor is superior to those of other reported MnO_2-based sensors (Table S2). In addition, there is no obvious difference when the same amount of DA is added in various ways (Fig. S10), suggesting an excellent accuracy of the sensor. Some co-existent interferences such as amino acids (Threonine, Tyrosine, L-cysteine and Lysine), ascorbic acid (AA), uric acid (UA), glucose, certain inorganic salts ($NaNO_3$, KCl, $NaNO_2$ and KIO_3) and biogenic amines (epinephrine, adrenaline, histamine, serotonin, tyramine and phenethylamine) can not infulence the determinaion in 10-fold concentration of DA (Fig. 4D), indicating an

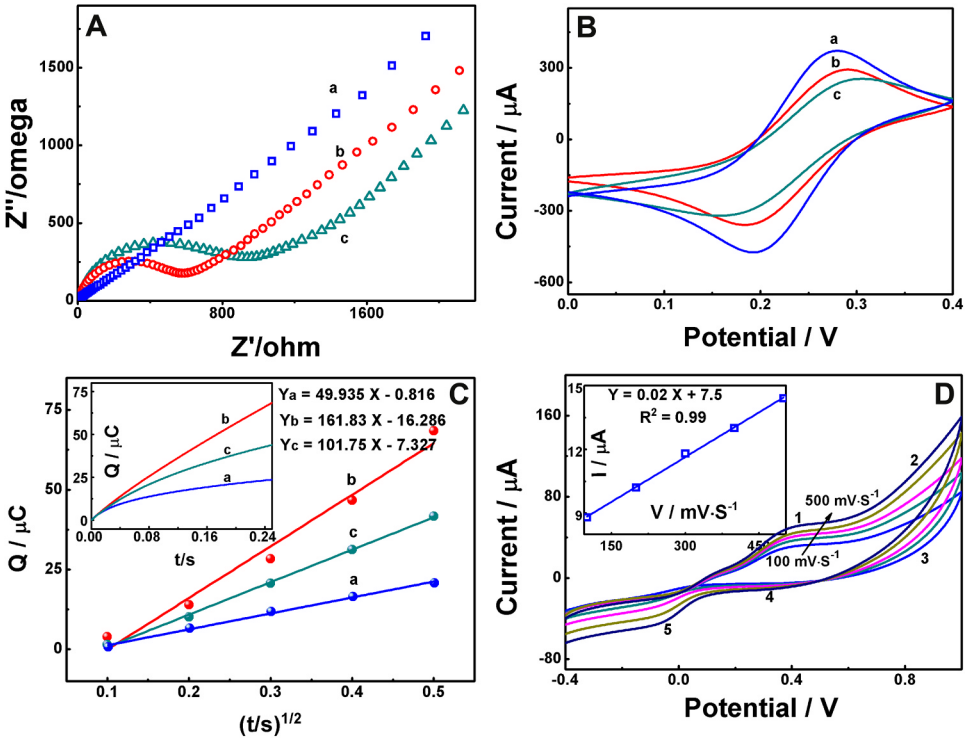

Fig. 3. Electrochemical properties of the modified electrodes: EIS (A) and CVs (B) in 5 mmol·L^{-1} $[Fe(CN)_6]^{-3/-4}$ (1:1) + 0.1 mol·L^{-1} KCl; (C) the curves of Q-t$^{1/2}$ and Q-t (inset) for reduction of 1 mmol·L^{-1} $K_3Fe(CN)_6$ in 2 mol·L^{-1} KCl; (D) CVs of Fe^{3+}@ε-MnO_2/GCE in phosphate buffer (pH 7.4) with 0.01 mmol·L^{-1} DA at various scan rates. Inset: oxidation peak currents vs. the scan rates (All the curves in A, B and C: a - GCE; b - Fe^{3+}@ε-MnO_2/GCE and c - α-MnO_2/GCE).

excellent selectivity of the modified electrode assembled in this work. Desirable stability and reproducibility of the sensor are also confirmed (Fig. S11).

3.4. Catalytic mechanism of hollow Fe^{3+}@ε-MnO_2 microspheres to dopamine

According to the phenomenon that anodic peak potential shifts to the negative direction linearly with the increase of pH value ranged from 5.6 to 8.6, we can know that the protons involve in the electrode reaction (Fig. S2A). The anodic peak potential is linearly proportional to the pH value with the equation as E_{pa} = -0.056 pH + 0.799 (R^2 = 0.99). The slope is caculated to be −0.056, which is colse to the theoretical value of −0.059 V/pH at room temperature, indicating that the number of electron-transfer and protons taking part in the reaction of DA oxidation process are equal.

CV curves of the constructed Fe^{3+}@ε-MnO_2/GCE electrode in DA aqueous solution (0.01 mmol·L^{-1}) tested at a designed scan rates

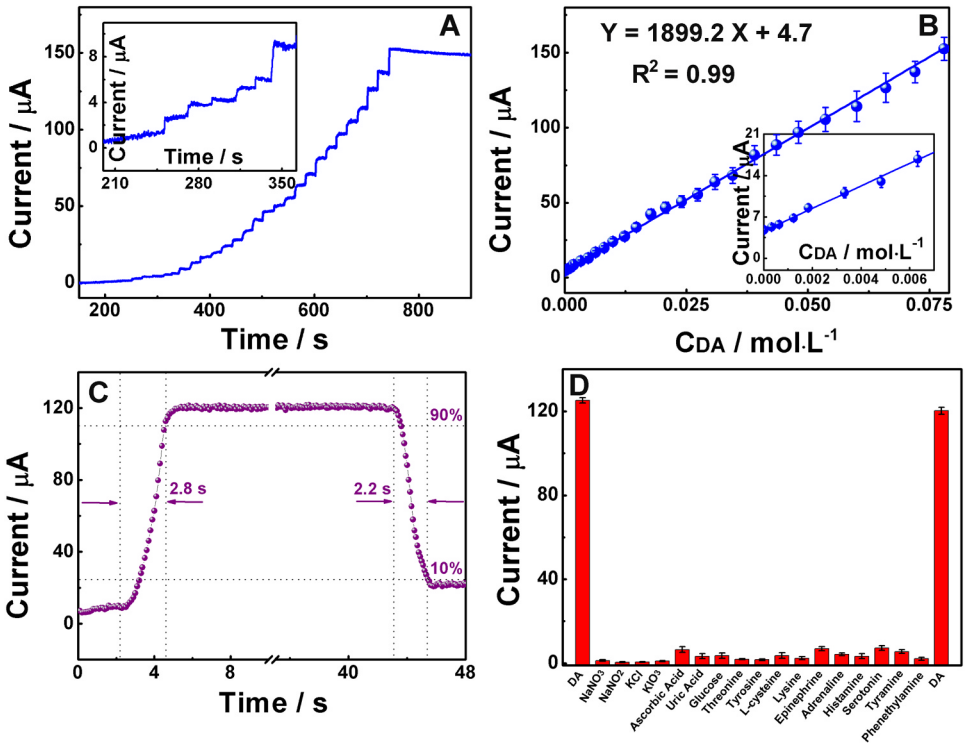

Fig. 4. (A) Current responses obtained from Fe^{3+}@ε-MnO_2/GCE in series of addition of DA in phosphate buffer (pH 7.4). Applied potential: 0.4 V (vs. SCE). Inset: magnified plot of the small ladders; (B) Calibration plot as a function of DA concentration. Inset: magnified plot of low analyte concentrations; (C) Response-recovery curve to 0.05 mol·L^{-1} DA; (D) Interference study in the presence of 0.05 mol·L^{-1} DA and 0.5 mol·L^{-1} interfering chemicals.

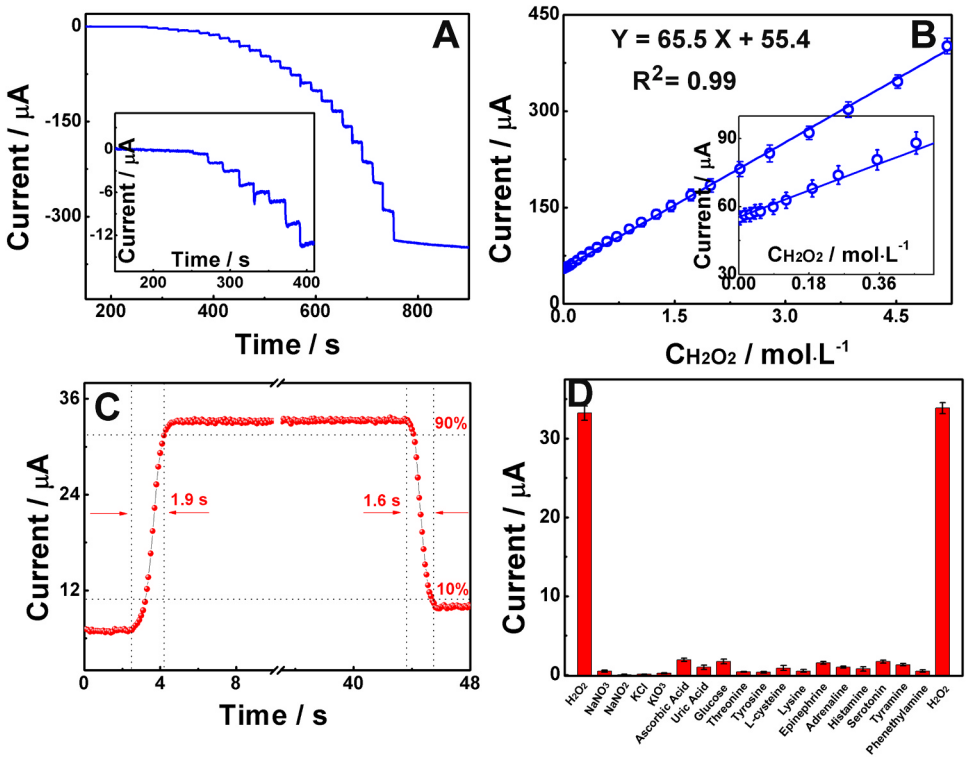

Fig. 5. (A) Current responses obtained from Fe^{3+}@ε-MnO_2/GCE in series of addition of H_2O_2 in phosphate buffer (pH 7.4). Applied potential: −0.4 V (vs. SCE). Inset: magnified plot of the small ladders; (B) Calibration plot as a function of H_2O_2 concentration. Inset: magnified plot of low analyte concentrations; (C) Response-recovery curve to 0.05 mol·L^{-1} H_2O_2; (D) Interference study in the presence of 0.05 mol·L^{-1} H_2O_2 and 0.5 mol·L^{-1} interfering chemicals.

(100–500 mV·s^{-1}) were applied to the investigation of electrochemical oxidation mechanism of DA. As shown in Fig. 3D, the oxidation peak current increases with the increasing of scan rate as well as the peak potentials shift positively, implying that DA oxidation occurred on the surface of Fe^{3+}@ε-MnO_2/GCE is an irreversible process. The associated current-scan rate relationship is: $I_{pa} = 0.0486\ \nu + 26.106$ (R^2 = 0.997). Based on the Randles-Ševčik formula (Liu et al., 2010), it could be a surface-controlled electron transfer kinetic process. The number of electron transferred in the reaction can be determined by the Laviron's equations:

$$I_p = \frac{n^2F^2\nu A\Gamma_T}{4RT} = \frac{nFQ\nu}{4RT}\ Q = nFA\Gamma_T \quad (2)$$

where n presents electrons transferred number; F is the Faraday constant; A is electrode area; Q is the peak area and ν is corresponding scan rate. Based on the relationship of I_p versus ν, the values of n are between 1.72 and 1.95, therefore, the values of n are approximately 2. Beyond that, the charge-transfer coefficient was also caculated. The corresponding equation is (Eq. (3)) (Liu et al., 2010)

$$E_p = E_0 + \frac{RT}{(1-\alpha)nF}\ln\nu \quad (3)$$

Where α is the charge-transfer coefficient and others have same meanings as above. The dependency of E_{pa} on ln ν for the oxidation of DA at Fe^{3+}@ε-MnO_2/GCE is depicted in Fig. S12, where the regression equation is $E_{pa} = 0.0296 \ln\nu + 0.465$ (R^2 = 0.992). The value of α is calculated as 0.56 through the slope of E_{pa} - ln ν.

Based on the results mentioned above, it can be inferred that two electrons and two protons participate in the DA oxidation process. According to the relative report (He et al., 2019), the mechanism of the electrocatalytic oxidation of DA may be the formation of semi-quinone radical intermediate at the first step (Eq. 4), following with the release of one electron and one proton. Subsequently, the quinone produced when one electron and one proton were further released from the above semi-quinone radical intermediate (Eq. 5). The mechanism can be described as follows:

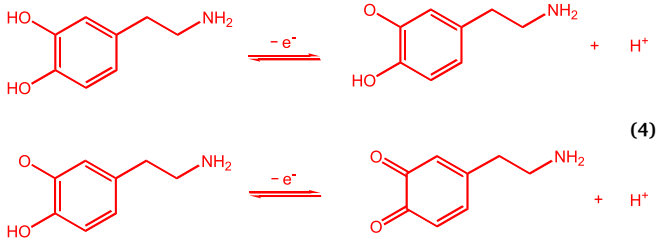

(4)

(5)

3.5. Electrocatalytic performance of Fe^{3+}@ε-MnO_2/GCE for H_2O_2

The Fe^{3+}@ε-MnO_2 also presents an ideal response to H_2O_2. The amperometric experiments of the Fe^{3+}@ε-MnO_2/GCE to different aliquots of H_2O_2 were operated using phosphate buffer (pH 7.4) under the buffer system at −0.4 V (Fig. 5A). This H_2O_2 sensor shows a desirable linear range from 0.000133 to 5.19 mmol·L^{-1} accompanied by a high sensitivity of 242.6 μA m(mol·L^{-1})$^{-1}$ cm^{-2} (Fig. 5B). The detection limit is 0.05 μmol·L^{-1} (S/N = 3). As described as Fig. 5C, the current almost achieves 90% level within 1.9 s, and it recovers to 10% of the base line within 1.6 s after a rapid dilution. The experimental results in this work are also compared with those of reported literatures (Table S3). 10-fold concentration of interferences such as glucose and ascorbic acid can not infulence the determinaion of H_2O_2 (Fig. 5D). The number of electron-transfer, protons, and charge-transfer coefficient in the reaction are 1, 1 and 0.14, respectively (Figs. S13–14). The reduction of H_2O_2 on Fe^{3+}@ε-MnO_2/GCE is also a surface-controlled electron transfer kinetic process (Fig. S14). Therefore, the reaction on the

Table 1
Determination of H_2O_2 and DA in biological samples using the Fe^{3+}@ε-MnO_2 modified glassy carbon electrode.

Sample	Hydrogen peroxide (μmmol L^{-1})			Dopamine (μmmol L^{-1})		
	added	found[a]	Recovery(%)[b]	added	found[a]	Recovery(%)[b]
Serum	50	48.7 ± 0.9	97.4 ± 1.0	20	19.1 ± 2.4	95.5 ± 2.5
	100	98.2 ± 0.9	98.2 ± 0.9	40	38.8 ± 1.2	97.0 ± 1.1
	150	145.8 ± 0.9	97.2 ± 1.0	60	58.3 ± 1.1	97.2 ± 1.2
Urine	50	47.9 ± 1.6	95.9 ± 1.4	20	18.7 ± 1.8	93.3 ± 1.9
	100	97.7 ± 1.2	97.7 ± 1.2	40	38.5 ± 1.5	96.2 ± 1.4
	150	147.1 ± 0.9	98.1 ± 1.0	60	58.2 ± 1.3	96.9 ± 1.5

[a] found = mean ± RSD. (n = 3) and RSD were all lower than 2.5%.
[b] Recovery(%) = 100% x (found amount – original amount)/added amount, where the amount of DA in the diluted serum and urine was 0.01 and 0.05 μmmol·L^{-1}, while H_2O_2 was not detected in above two original biological samples.

Fe^{3+}@ε-MnO_2/GCE can be described as follows:

$$1/2H_2O_2 \rightleftharpoons 1/2O_2 + H^+ + e^- \quad (6)$$

3.6. Determination of DA and H_2O_2 in biological samples

In view of the close relation of DA and H_2O_2 to the health of organisms, accurate detection of the above two components in biological samples is very important. The real samples of serum (centrifuged) and urine were diluted 40 times with phosphate buffer (pH 7.4) in this experiment. The DA and H_2O_2 were brought into real samples with the usage of standard addition method at three different levels, with all samples prepared and analyzed in triplicate. The results indicate that the sensor is excellent and can be successfully applied to the detection of DA and H_2O_2 in biological samples (Table 1).

4. Conclusions

Hollow hydrangea-like Fe^{3+}@ε-MnO_2 microspheres have been successfully prepared by one-step hydrothermal method. The sensor based on these microsphers exhibits excellent catalytic performance to DA and H_2O_2, including high response, good selectivity, low detection limit, good linear range, and short response time. The reason may be the unique structure and doping of Fe^{3+}, which provides a high conductivity and larger specific surface area accompanied by more active sites. The number of electron-transfer, protons and charge-transfer coefficient in the oxidation process of DA is 2, 2, and 0.56, while that in the reduction process of H_2O_2 is 1, 1 and 0.14, respectively. The sensor exhibits satisfactory performance towards the determination of DA and H_2O_2 in serum and urine samples, indicating a potential application in biological samples detection.

CRediT authorship contribution statement

Haiyan Song: Writing - original draft. **Hui Zhao:** Data curation. **Xianfa Zhang:** Data curation. **Yingming Xu:** Project administration. **Xiaoli Cheng:** Validation. **Shan Gao:** Writing - review & editing. **Lihua Huo:** Methodology.

Acknowledgments

This work was supported by the National Natural Science Foundation of China (21771060, 61271126, and 21305033), International Science & Technology Cooperation Program of China (2016YFE0115100), Program for Science and Technology Project of Heilongjiang province (B2015008).

Credit author statement

This work was accomzplished by seven authors, in which Lihua Huo conducts the methodology, Yingming Xu is responsible for the project adminstration, Haiyan Song conducts the writing- original draft, Hui Zhao and Xianfa Zhang provide data curation, Xiaoli Cheng is responsible for validation and Shan Gao performes the writing- review & editing.

Conflict of interest

We declare that we have no financial and personal relationships with other people or organizations that can inappropriately influence our work, there is no professional or other personal interest of any nature or kind in any product, service and/or company that could be construed as influencing the position presented in, or the review of, the manuscript entitled “3D hierarchical hollow hydrangea-like Fe^{3+}@ε-MnO_2 microspheres with excellent electrochemical performance for dopamine and hydrogen peroxide”.

Appendix A. Supporting information

Supplementary data associated with this article can be found in the online version at doi:10.1016/j.bios.2019.03.017.

References

Chi, M.Q., Zhu, Y., Jing, L.W., Wang, C., Lu, X.F., 2019. Talanta 191, 171–179.
Dai, H.X., Chen, Y.L., Niu, X.Y., Pan, C.J., Chen, H.L., Chen, X.G., 2018. Biosens. Bioelectron. 118, 36–43.
Dong, S., Xi, J.B., Wu, Y.N., Liu, H.W., Fu, C.Y., Liu, H.F., Xiao, F., 2015. Anal. Chim. Acta 853, 200–206.
Dong, Y.Y., Zhang, L., 2018. Electrochim. Acta 271, 27–34.
He, Y.S., Pan, C.G., Cao, H.X., Yue, M.Z., Wang, L., Liang, G.X., 2018. Sens. Actuators B 265, 371–377.
Jaiswal, N., Tiwari, I., Foster, C.W., Banks, C.E., 2017. Electrochim. Acta 227, 255–266.
Jin, H., Zhao, C.Q., Gui, R.J., Gao, X.H., Wang, Z.H., 2018. Anal. Chim. Acta 1025, 154–162.
Kumar, D.R., Kesavan, S., Baynosa, M.L., Nguyen, V.Q., Shim, J.J., 2018. J. Colloid Interfaces Sci. 530, 361–371.
Li, J.H., Jiang, J.B., Liu, Mq, Xu, Z.F., Deng, P.H., Qian, D., Tong, C.Y., Xie, H.B., Yang, C.M., 2017. Anal. Chim. Acta 985, 155–165.
Li, Z.Q., Ding, Y., Xiong, Y.J., Yang, Q., Xie, Y., 2005. Chem. Commun. 7, 918–920.
Lin, M., Chen, B.L., Wu, X., Qian, J.S., Fei, L.F., Lu, W., Helen Chan, L.W., Yuan, J.K., 2016. Nanoscale 8, 1854–1860.
Lin, M.T., Beal, M.F., 2006. Nature 443, 787–795.
Liu, L.H., Duan, C.Q., Gao, Z.N., 2010. Croat. Chem. Acta 83, 409–414.
Liu, J., Meng, L.J., Fei, Z.F., Dyson, P.J., Zahng, L., 2018. Biosens. Bioelectron. 121, 159–165.
Niu, B.B., Jin, F.J., Zhang, L.L., Shen, P.F., He, T.M., 2018. Electrochim. Acta 263, 217–227.
Pargoletti, E., Cappelletti, G., Minguzzi, A., Rondinini, S., Leoni, M., Marelli, M., Vertova, A., 2016. J. Power Sources 325, 116–128.
Rao, D.J., Zhang, X.J., Sheng, Q.L., 2016. Microchim. Acta 9, 2597–2604.
Revathi, C., Rajendra Kumar, R.T., 2017. Electroanalysis 29, 1481–1489.

Saraf, M., Natarajan, K., Mobin, S.M., 2018. ACS Sustain. Chem. Eng. 6, 10489–10504.
Song, H.Y., Ni, Y.N., Kokot, S., 2014. Biosens. Bioelectron. 56, 137–143.
Sha, R., Vishnu, N., Badhulika, S., 2018. Microchim. Acta 185. https://doi.org/10.1007/s00604-018-2927-y.
Sinha, L., Pakhira, S., Bhojane, P., Mali, S., Hong, C.K., Shirage, P.M., 2018. ACS Sustain. Chem. Eng. 6, 13248–13261.
Song, H.Y., Ni, Y.N., Kokot, S., 2013. Microchim. Acta 180, 1263–1270.
Tran, D.T., Hoa, V.H., Tuan, L.H., Kim, N.H., Lee, J.H., 2018. Biosens. Bioelectron. 119, 134–140.
Thanh, T.D., Balamurugan, J., Tuan, N.T., Jeong, H., Lee, S.H., Kim, N.H., Lee, J.H., 2017. Biosens. Bioelectron. 89, 750–757.
Wang, Z.Y., Wang, F.P., Li, Y., Hu, J.L., Lu, Y.Z., Xu, M., 2016. Nanoscale 8, 7309–7319.
Wu, Z.L., Sun, L.P., Zhou, Z., Li, Q., Huo, L.H., Zhao, H., 2018. Sens. Actuators B 276, 142–149.
Xiao, T., Sun, J., Zhao, J.H., Wang, S., Liu, G.Y., Yang, X.R., 2018. ACS Appl. Mater. Interfaces 10, 6560–6569.
Zhang, C., Ren, J.J., Zhou, J.X., Cui, M., Li, N., Han, B.K., Chen, Q., 2018. Analyst 143, 3075–3084.
Zheng, X.Y., Yu, L., Lan, B., Cheng, G., Lin, T., He, B.B., Ye, W.J., Sun, M., Ye, F., 2017. J. Power Sources 362, 332–341.